Supplementary Material for: Droplet splashing on curved substrates

Thomas C. Sykes,[1,*] Ben D. Fudge,[1] Miguel A. Quetzeri-Santiago,[2]
J. Rafael Castrejón-Pita,[3,†] and Alfonso A. Castrejón-Pita[1,‡]

[1] *Department of Engineering Science, University of Oxford, Oxford OX1 3PJ, United Kingdom*
[2] *Mesoscale Chemical Systems Group, MESA+ Institute and Faculty of Science and Technology, University of Twente, 7500AE Enschede, The Netherlands*
[3] *School of Engineering and Materials Science, Queen Mary University of London, London E1 4NS, United Kingdom*

(Dated: January 11, 2022)

CONTENTS

§1. ACCOUNTING FOR NON-SPHERICITY OF IMPACTING DROPLETS

A. Measuring the radius of curvature, r_c

As mentioned in the main text, oscillations in the free surface of the falling droplets meant that they were not necessarily spherical on impact. In such cases, several studies in the literature [e.g. 1] have recognised that it is more appropriate to base the characteristic length upon the radius of curvature at the bottom of the droplet (its 'south point'), r_c, rather than use the droplet's equivalent spherical radius, r_n. If the droplet can be well approximated by an axially-aligned ellipse, then r_c is well-defined by the droplet's aspect ratio and r_n. However, the droplets in this study could not always be well approximated by such an ellipse, so it was preferred to measure r_c directly using image processing: a circle was fitted to detected edges within a certain angular range around the droplet's south point.

For a typical experiment, Fig. S1a demonstrates the result of fitting a (blue) circle to all (yellow) detected edges of the droplet, which suggests that $r_n = 0.96\,\text{mm}$ in this example. Evidently, the droplet is oblate (with eccentricity ~ 0.29); the fitted circle does not coincide with the detected edges around the south or east points, but this fitting is likely to yield a fair approximation to r_n. In Fig. S1b, a (red) circle is fitted only to the (green) detected edges spanning the lower 60° of detected edges (called the 'fitting angular range around the south point'), yielding $r_c = 1.06\,\text{mm}$. In this case, the fitted circle coincides exceptionally well with the detected edges around the south point, giving high confidence that r_c approximates the radius of curvature of the bottom of the droplet well.

The choice of 60° for the fitting angular range is elucidated in Fig. S1c, where r_c is measured based upon angles of 20°–120° for six randomly-chosen experiments, represented by different colours. For each experiment, r_n is indicated by the dashed line of equivalent colour. For small angular ranges $\lesssim 40°$, the measurement of r_c is unreliable due to the small range in vertical position of all detected edge pixels involved, relative to the error in their detected position,

* thomas.sykes@eng.ox.ac.uk; t.c.sykes@outlook.com
† castrejon@cantab.net
‡ alfonso.castrejon-pita@wadham.ox.ac.uk

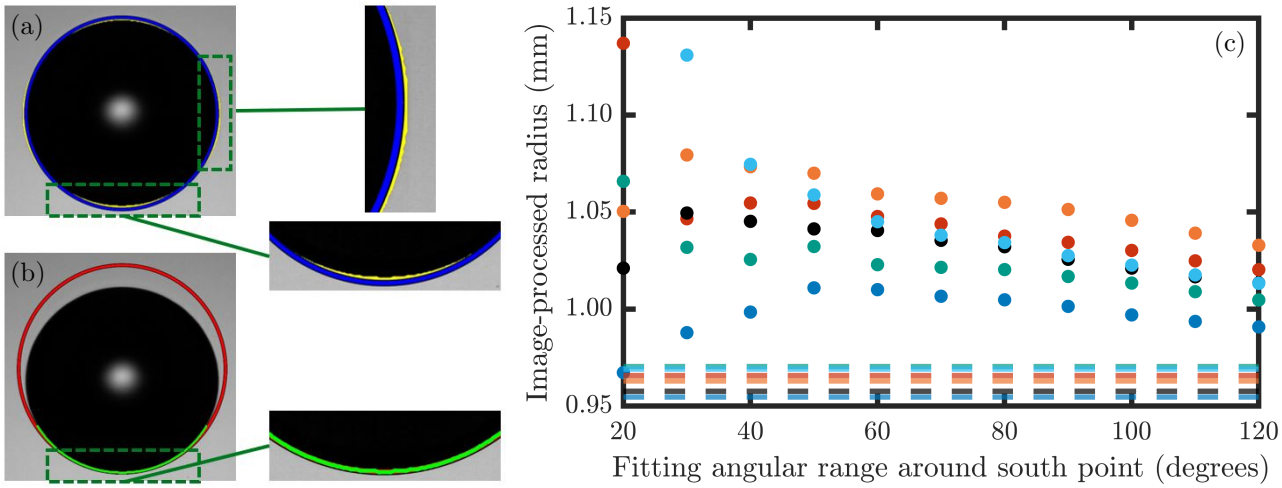

FIG. S1: (a) A (blue) circle fitted to the (yellow) detected edges of the whole droplet, yielding $r_n = 0.96\,\text{mm}$. (b) A (red) circle fitted to the (green) detected edges of the same droplet, covering an angular range of 60° spanning the droplet's south point, yielding $r_c = 1.06\,\text{mm}$. (c) The dependence of r_c on fitting angular range for six randomly-chosen experiments, represented by different colours; the horizontal dashed lines indicate r_n for each.

despite the use of an accurate subpixel edge detection method (see Ref. [2]). On the other hand, the oblate nature of a typical droplet in this work means that the use of a too high angular range would be expected to artificially lower the detected r_c (and similarly, if the droplet were a prolate spheroid, increase the measured r_c), which is borne out in Fig. S1c. 60° is therefore chosen as a good compromise between these two competing demands – it's the lowest value with which we have confidence of consistently attaining reliable measurements. In general, the choice of angular range is likely to depend upon the effective resolution of the image, magnitude of eccentricity, and quality of edge detection.

B. Effects of non-sphericity

The axisymmetric impact of three $r_n = 0.96\,\text{mm}$ droplets onto a $r_s = 2.5\,\text{mm}$ sphere at $u = 2.40\,\text{m}\,\text{s}^{-1}$ are shown in Fig. S2. $r_c \in [1.02, 1.06]$ mm is varied between rows, giving $\text{We} = \rho u^2 \cdot 2r_c/\sigma \in [412, 430]$. The smallest $r_c = 1.02\,\text{mm}$ droplet exhibits simple deposition (no breakup), whilst the two more oblate droplets ($r_c \in \{1.04, 1.06\}$ mm) splash. If the characteristic length scale were based upon r_n, then there would be no difference in Weber number (or indeed

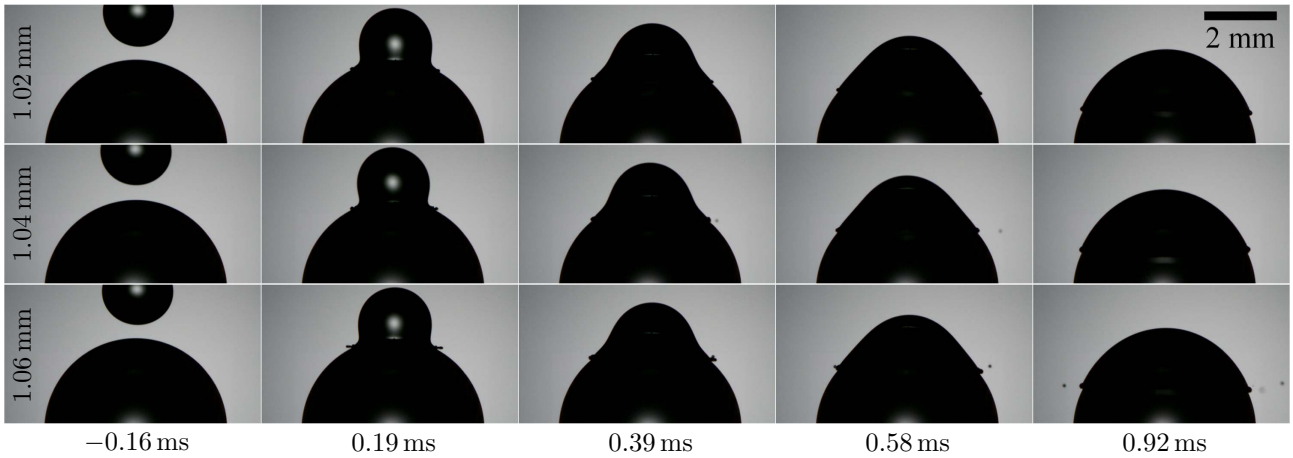

FIG. S2: A collection of three $r_n = 0.96\,\text{mm}$ droplets impacting a $r_s = 2.5\,\text{mm}$ sphere at $u = 2.40\,\text{m}\,\text{s}^{-1}$. Only r_c (indicated in each row) is varied between each row, spanning the splashing threshold: We = 412 (no splashing), We = 423 (one satellite droplet) and We = 430 (several satellites), respectively.

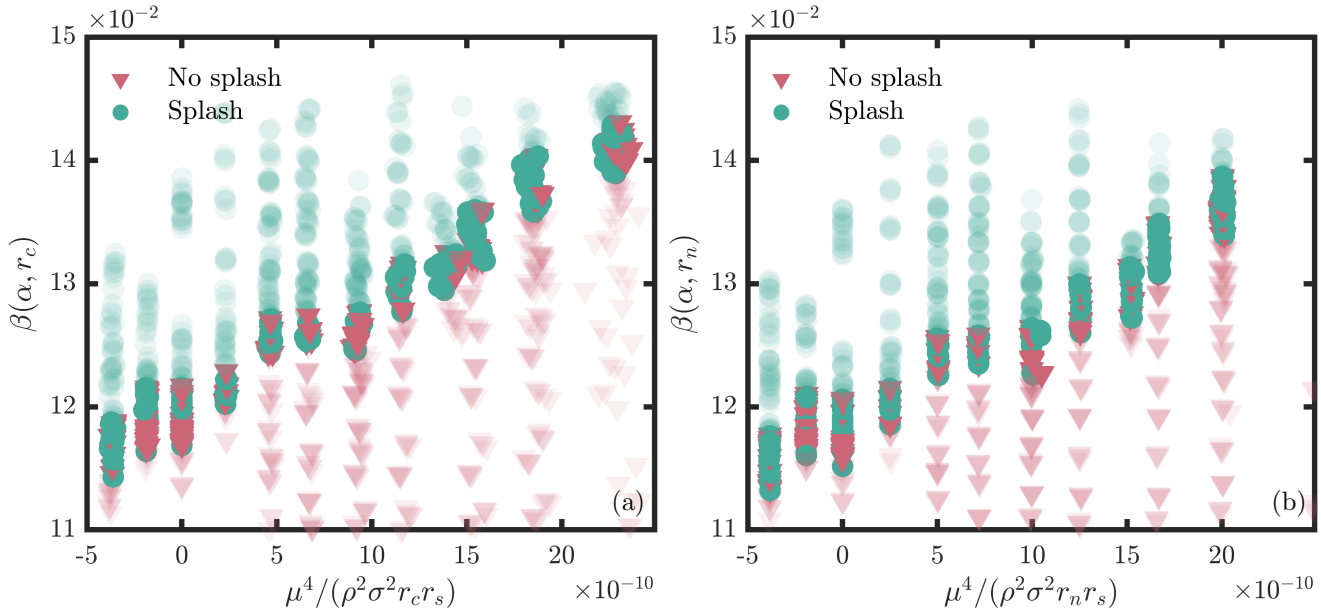

FIG. S3: Splashing propensity of (3.6 ± 0.3) µL and (4.85 ± 0.15) µL droplets, in terms of the (uncorrected) splashing ratio, $\beta(\alpha)$. (a) The length scale is r_c; the graph is a repeat of Fig. 3b in the main text. (b) The length scale is r_n.

$\beta(\alpha)$ and K) between these three experiments. However, using r_c enables the impact outcomes to be appropriately divided.

Figure. 3b (main text) also appears as Fig. S3a here. Recall that this graph is based upon the length scale r_c. For comparison, these data are replotted in Fig. S3b, using r_n as the length scale. Both graphs in Fig. S3 show the same qualitative trend, though they are quantitatively distinct. Note the lower random variation in r_n than r_c, which manifests as more clearly defined columns in the latter panel of Fig. S3. Nevertheless, the threshold regions are generally slightly extended when using r_n, further indicating the appropriateness of using r_c as the length scale in this work (i.e. the choice reduces the effective error).

§2. DETAILED EXPERIMENTAL INFORMATION

A. Droplet generation procedure

As noted in the main text, droplets were generated by dripping in this work. Since the substrate was spatially varying, precise control of the droplet impact position was required, unlike for geometrically and chemically-homogeneous substrates. To achieve impact velocities relevant to splashing, especially for the smaller spheres, the tip had to be positioned high above the substrate, which posed challenges in attaining and maintaining the desired impact position. The following procedures were employed to reduce the random variation in droplet impact position:

- An extra droplet was generated (and caught) immediately before each droplet was deposited onto the substrate, with the second droplet found to be more predictable in terms of impact position.
- The tip was covered by a loosely-fitting cylindrical pipe to protect the falling droplet from random air currents during its initial fall. Protecting the droplet's path closer to the tip (where its velocity was low) was found to be far more important than protecting its path close to the substrate, so an approximately $15 - 30$ cm telescopic tube was usually used.
- Dewetting of the tip during periods that the syringe pump was not active for more than a minute or so (e.g. during height changes or offloading data from the cameras) was found to greatly influence subsequent impact positions. Therefore, the syringe pump was programmed to activate for (4 ± 1) s in every 20 s when it would otherwise be inactive, in order to maintain the meniscus at the end of the tip and keep the tip wetted throughout.

Taken together, these procedures enabled adequate control of droplet impact positions.

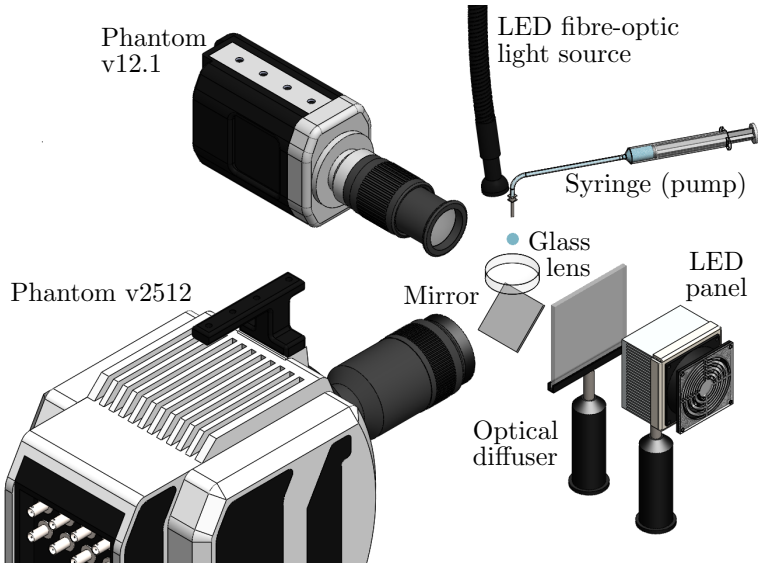

FIG. S4: A sketch (not to scale) of the experimental setup used for concave surfaces. The glass lens (concave substrate) was supported on a horizontal platform (not shown), in which a hole was cut to provide optical access.

B. Imaging

The cameras used in this work are detailed in the main text, which are the v2512, TMX 7510, Miro LAB310 and v12.1 (all Phantom high-speed cameras from Vision Research/AMETEK). Table S1 lists the lenses used with these cameras, alongside the pertinent imaging parameters (frame rate, effective resolution and exposure time). For all experiments, a 30 W LED array provided illumination via a ground glass diffuser to the v12.1/Miro, whilst a Photonic F5100 LED fibre-optic light source was used with a diffuser (except for the concave experiments) for the v2512/TMX.

C. Experimental setup for concave substrates

The experimental setup used for concave surfaces ($r_s < 0$) is shown in Fig. S4. A Phantom v2512 captured the impact and splashing dynamics from below (through the substrate) via an optical mirror, at up to 39,000 fps and with an effective resolution of 107 pixels mm^{-1}. Illumination for this camera was provided by an LED fibre-optic light source (Photonic F5100) positioned close to the dispensing tip, with the light path into the lens offset by a small angle (in the vertical plane) to the path of the falling droplet. To determine the droplet's geometry and impact velocity, a Phantom v12.1 was positioned perpendicular to the v2512 and captured the droplet as it fell into the lens, at up to 11,000 fps and with an effective resolution of 98 pixels mm^{-1}. Both cameras were kept horizontal, meaning that the latter lost sight of the droplet up to 7 mm above the substrate's apex. As for convex substrates, the impact velocity was determined from a second-order polynomial fit to the time series of the droplet's south-point height (relative to the substrate), evaluated at the substrate without the impact time needing to be known a priori. The impact velocities were found to be consistent with the $> 1,000$ convex substrate experiments in which the droplet could be seen up to and beyond the moment of impact at $t = 0$.

TABLE S1: Lenses and characteristics of the imaging configurations used in this work.

Camera	Lens	Ext. tubes (mm)	Frame rates (fps)	Effective res. (pixels mm^{-1})	Exposure (µs)
v2512	Nikon AF-S VR 105 mm f/2.8G	92 – 124	25,000 – 40,000	105 – 131	0.8 – 2.4 (convex) 20 (concave)
TMX		92	94,000	169	2.3
TMX	Navitar 12X Zoom Lens System[a]	0	76,000; 110,000	199	0.8 – 1.2
Miro	Nikon AF 60 mm f/2.8D	0	7,200	34	2.3
v12.1	Laowa 100 mm f/2.8 2x APO	20 – 36	10,200; 11,000	48 – 99	18 – 25

[a] Only used for qualitative data (no experiments using this lens are seen in the regime maps).

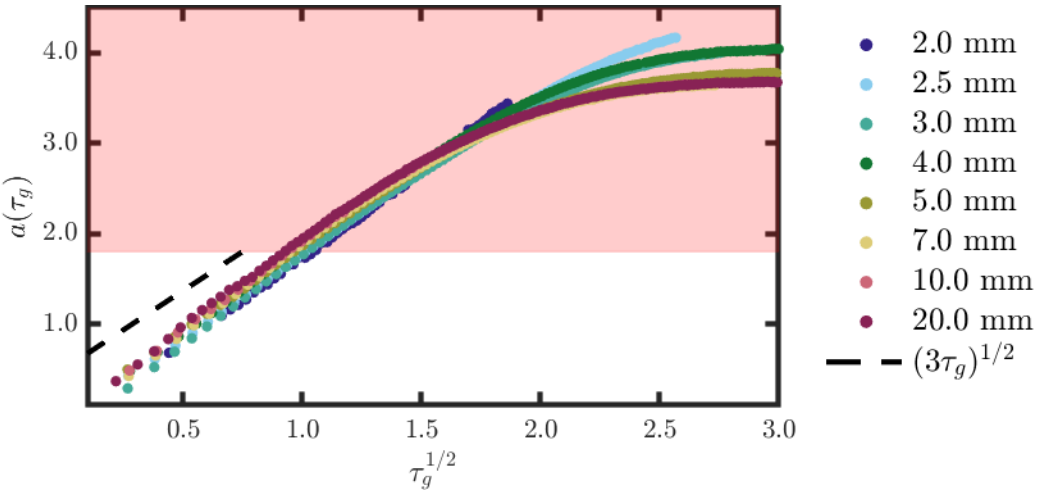

FIG. S5: Dimensionless half spread length, $a(\tau_g)$ of droplets spreading along the surface of a spherical substrate (r_s values are indicated in the legend) following axisymmetric impact at We $= 276 \pm 6$. Times τ_g are dimensionless with respect to the kinetic time scale using the droplet radius r_c as the length scale, r_c/u. The dashed line indicates the expected gradient for flat substrates – i.e. $(3\tau_g)^{1/2}$, translated upwards by 0.5 units for improved visibility. The red region indicates spread lengths beyond the expected point of breakup for experiments that splash.

§3. SPREADING OF DROPLETS ON SPHERICAL SUBSTRATES

For a flat substrate, the dimensionless half spread length of the droplet (in other words, the radius of the wetted area), a, is given by $a(\tau_g) = (3\tau_g)^{1/2}$, where $t/\tau_g = r_c/u$. The latter is the kinetic time scale based upon the droplet radius, rather than the diameter. The flat-substrate relation for a is derived from Wagner's theory, and has been extensively validated [3].

To check whether substrate curvature affects spreading in the period of interest for droplet splashing (i.e. before breakup occurs, if it would), we consider the time series of $a(\tau_g)$ for each spherical substrate studied. A representative We $= 276 \pm 6$ experiment for each such substrate is chosen, and $a(\tau_g)$ plotted against $\tau_g^{1/2}$ in Fig. S5. These Weber numbers are close to the splashing threshold for a flat substrate (so no experiment plotted splashes), chosen to reduce error in determining the contact line position (satellites and long extensive lamellae can obscure the true contact line – see Fig. 5a in the main text). Similar graphs can be observed for all Weber numbers studied. The red shaded region in Fig. S5 indicates spread lengths above which lamella breakup would have occurred (recall that $s = 1.9\,\text{mm}$ from Sec. 3B), so this region is not of interest from the perspective of splashing thresholds.

Figure S5 shows that substrates of all (positive) curvatures studied have very similar spreading rates up to $a(\tau_g) \approx 2.5$, which is well into the red region of irrelevance to splashing thresholds. Moreover, the spreading dynamics at times of interest follow the expected $(3\tau_g)^{1/2}$ behaviour seen for flat substrates – see the dashed line (translated upwards by 0.5 units to improve its visibility) and compare its gradient to the data for spheres. Hence, substrate curvature appears not to affect spreading dynamics during the (relatively short) period of time relevant to splashing thresholds.

§4. LIST OF OTHER SUPPLEMENTARY MATERIAL

Figure 1 videos: fig1_{2,3,4,7,20}mm.mp4 and fig1_flat.mp4
Videos to accompany each experiment shown in Fig. 1. The videos cover dimensionless times $\tau \in [-0.3, 1.6]$ ($\tau \in [-0.3, 1.2]$ for the flat substrate) and play approximately 3,300x slower than real time. The width of each $r_s > 0$ video (in physical units) is matched to have a common effective scale. The substrate radius of curvature, r_s, is indicated in the file name of each video.

Regime map raw data: fig{3a,3b,6}_points.csv
Comma-separated value (CSV) files containing a list of our data points contained within each figure indicated in the file name. Each row corresponds to a different data point. The first column indicates the substrate's radius of

curvature (in millimeters) – 0 is used to identify flat substrates, for which $r_s \to \infty$; 300 identifies the larger droplet volume data, for which $r_s = 3.0\,\mathrm{mm}$. The final column indicates the splashing outcome in terms of MATLAB markers: 'v' indicates no splashing, whilst 'o' indicates splashing.

Regime map threshold data: fig{3a,3b,6}_thresholds.csv
CSV files containing the vertical axis values delineating each substrate's splashing threshold region for each regime map. The first column (substrate radius of curvature) follows the same conventions as for the raw data (see above).

---

[1] E. Li, M.-J. Thoraval, J. Marston, and S. T. Thoroddsen, Early azimuthal instability during drop impact, J. Fluid Mech. **848**, 821 (2018).

[2] A. Trujillo-Pino, K. Krissian, M. Alemán-Flores, and D. Santana-Cedrés, Accurate subpixel edge location based on partial area effect, Image Vision Comput. **31**, 72 (2013).

[3] G. Riboux and J. M. Gordillo, Experiments of drops impacting a smooth solid surface: A model of the critical impact speed for drop splashing, Phys. Rev. Lett. **113**, 024507 (2014).